

Dual-Band Circularly Polarized Fully Reconfigurable Reflectarray Antenna for Satellite Applications in the Ku Band

Baladi, Elham; Xu, Min Yin; Faria, Nicolas; Nicholls, Jeff; Hum, Sean V.

DOI

[10.1109/TAP.2021.3090577](https://doi.org/10.1109/TAP.2021.3090577)

Publication date

2021

Document Version

Accepted author manuscript

Published in

IEEE Transactions on Antennas and Propagation

Citation (APA)

Baladi, E., Xu, M. Y., Faria, N., Nicholls, J., & Hum, S. V. (2021). Dual-Band Circularly Polarized Fully Reconfigurable Reflectarray Antenna for Satellite Applications in the Ku Band. *IEEE Transactions on Antennas and Propagation*, 69(12), 8387-8396. <https://doi.org/10.1109/TAP.2021.3090577>

Important note

To cite this publication, please use the final published version (if applicable). Please check the document version above.

Copyright

Other than for strictly personal use, it is not permitted to download, forward or distribute the text or part of it, without the consent of the author(s) and/or copyright holder(s), unless the work is under an open content license such as Creative Commons.

Takedown policy

Please contact us and provide details if you believe this document breaches copyrights. We will remove access to the work immediately and investigate your claim.

Dual-Band Circularly Polarized Fully Reconfigurable Reflectarray Antenna for Satellite Applications in the Ku Band

Elham Baladi, *Member, IEEE*, Min Yin Xu, *Student Member, IEEE*, Nicolas Faria, *Student Member, IEEE*, Jeff Nicholls, *Member, IEEE*, and Sean V. Hum, *Senior Member, IEEE*

Abstract—This work presents the design and experimental validation of a dual-band fully reconfigurable circularly polarized (CP) reflectarray (RA) antenna for satellite communication applications in the Ku band. The proposed structure operates with the downlink and uplink beams at frequency bands of [10.8–11.8] GHz and [14–15.4] GHz, respectively. Simultaneous and independent beam control is provided over each of the two bands. The constituent unit cell is composed of two interleaved circular loops of different sizes to address the two frequency bands. Each loop is loaded using four varactor diodes. The loops are symmetrically loaded in the transverse plane to provide an isotropic response suitable for CP applications. A phase range of more than 300° is achieved in both bands as the capacitive loading varies, with an average of 2 dB loss in the lower frequency band and 3 dB loss in the higher band. In this paper, the response of the unit cell is studied through full-wave simulations and verified through quasi-optical (QO) measurements, and the fully tunable performance of the reflectarray is validated through measurements in a near-field anechoic chamber.

Index Terms—reconfigurable reflectarrays, dual-band, circular polarization, continuously tunable, satellite communication, Ku band, antenna arrays.

I. INTRODUCTION

Wireless communication systems, including but not limited to, satellite communication systems, radars, and point-to-point terrestrial links can benefit from adaptive beam-forming through reconfigurable antennas. Although conventional reflectarrays (RAs) and transmitarrays (TAs) offer a simple solution for producing high-gain pencil beams, most designs are fixed and require mechanical scanning to address adaptive beam-forming requirements. Phased array antennas, on the other hand, provide versatile control in the excitation of their elements, allowing for reconfigurable beam-steering. Nevertheless, they often possess a large overall size and cost as each element requires a separate phase shifter module. Furthermore, the efficiency of phased arrays decreases as frequency increases towards the mm-wave regime, due to the use of transmission-line feed networks that become more lossy at higher frequencies [1]. Reconfigurable reflectarrays (RAs) and transmitarrays (TAs) have attracted significant research interest in recent decades, as they combine interesting features of passive RAs/TAs and electronically tunable properties of phased arrays. Reconfigurability is achieved through the introduction of electronically tunable discrete elements such as

varactor diodes, PIN diodes, and micro-electro-mechanical-systems (MEMS) switches within the unit cells [1], [2]. These components are controlled electronically to provide the required phasing between antenna elements in order to address the desired beam-forming scheme.

Satellite communication in the Ku band imposes several requirements on the antenna, such as a dual polarization response, simultaneous transmit/receive operation in the two bands and high isolation between the co- and cross-polar response. While parabolic reflectors meet these criteria, they are bulky and rely on mechanical scanning to address different beam directions. These drawbacks make electronically tunable RA antennas attractive alternatives, as they are lightweight and enable fast and versatile beam-scanning without the need for mechanical beam-pointing systems. Various passive CP RAs have been studied previously [3]–[14]. Single-band reconfigurable RAs have also been successfully implemented by relying on electronically tunable elements such as RF MEMS switches [15]–[18], PIN diodes [3], [19], [20] and varactor diodes [21]–[23]. Nonetheless, the design of *fully* reconfigurable *dual-band* CP RAs, although somewhat explored [24]–[26], has remained a challenge. The majority of recent efforts in implementing reconfigurable antenna arrays rely on PIN diodes and MEMS switches providing 1- or 2-bit phase control [19], [24], [27]–[30]. Electronically tunable designs depending on switches can have limited phase resolution, and therefore, degree of controllability. For example, a sequential rotation principle has been applied to split ring resonators that are loaded using RF MEMS switches [24]. A sequential rotation principle states that a rotation angle of ϕ inside the unit cell results in the phase shift of 2ϕ in the phase of the reflection parameter. Consequently, the use of six MEMS switches yields a phase resolution of only 120° . Following this rule, a phase resolution of 90° requires eight switches; this imposes a major limit on improving the tuning resolution especially at higher frequencies, where there are major constraints on the available physical space.

This work presents the design a dual-band dual-CP reconfigurable RA in the Ku band for user terminal applications in satellite communication systems, expanding on an earlier presentation of the unit cell response [31]. The aforementioned work discusses the unit cell and its magnitude/phase response under a uniform bias voltage. Since the proposed RA is electronically tunable, the nonuniform array design is in fact carried out after fabrication, through the calculation and application of the corresponding voltages for beamsteering. As such, the in-depth details of fabrication, the bias network and active design scheme, and experimental verification of

E. Baladi is with Syntronic R&D, Ottawa, ON, Canada. N. Faria and S. V. Hum are with the Edward S. Rogers Sr. Department of Electrical and Computer Engineering, University of Toronto, Toronto, ON, Canada. M. Y. Xu is with Delft University of Technology, Delft, Netherlands. J. Nicholls is with Kepler Communications Inc, Toronto, ON, Canada.

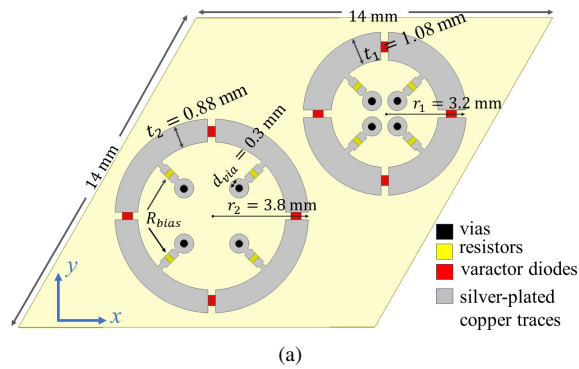


Fig. 1. Top view of the dual-band CP RA unit cell.

TABLE I
DESIGN PARAMETER DEFINITIONS AND VALUES FOR THE PROPOSED RA UNIT CELL

Parameter	Definition	Value
r_1	radius of the smaller loop	3.2 mm
r_2	radius of the larger loop	3.8 mm
t_1	trace width of the smaller loop	1.08 mm
t_2	trace width of the larger loop	0.88 mm
d_{via}	diameter of the via	0.3 mm
R_{bias}	resistance of bias resistors	25 k Ω

beamsteering behaviour in both operating bands are fully studied in this journal paper. The proposed prototype produces individually steerable pencil beams in downlink and uplink frequency bands of [10.8 – 11.8] GHz and [14 – 15.4] GHz, while allowing a continuous beam control in the angular range of $\pm 50^\circ$ from broadside in both operating bands.

This paper is organized as follows: Sec. II presents the design of the unit cell as well as the choice of the array grid. Sec. III shows the simulation data on the magnitude and phase response of the RA in both operating bands. The fabrication considerations and requirements as well as details of the control system are discussed in Sec. IV. Sec. V presents experimental data on the magnitude and phase response of the unit cell obtained through quasi-optical measurements along with the far-field response of the RA in both bands. The gain of the RA is also obtained in both bands and shown in Sec. V, wherein the details of different sources of loss are also outlined. Conclusions as well as future directions of this work are discussed in Sec. VI.

II. UNIT CELL DESIGN

The goal of this work is to present a unit cell with a symmetric CP response, whereby tunable behaviour can be obtained under either right-hand circular polarization (RHCP) or left-hand circular polarization (LHCP) excitations. In this scenario, the feed would be responsible for determining the sense of the polarization. The approach adopted here to design a dual-band dual-CP continuously tunable RA unit cell is based on the concept of tunable resonators. The unit cell needs to be capable of generating symmetric responses under vertical and horizontal linear polarizations (i.e. an isotropic response) at two different operating frequencies. Consequently, a symmetric unit cell structure is needed. Here, a loop-shaped

element is chosen, but it is worth noting that this choice is not unique and other symmetric structures such as squares and crosses would also meet this condition. In this work, loop-shaped resonators are chosen due to their fully symmetric geometry and stable angular response. In addition, loops are straightforward to interleave so as to minimize their mutual coupling.

The proposed dual-band RA unit cell is demonstrated in Fig. 1, which is composed of two circular loops for operation in the two bands, placed in an interleaved manner. Each loop is loaded through four uniformly spaced varactor diodes sharing an identical bias voltage. A MACOM MAVR-011020-1411 varactor diode model is chosen [32], which provides a capacitance of 0.04 to 0.27 pF inversely related to bias voltage values of 0 to 15 V. By controlling the capacitance electronically, the resonance frequency of the loop element is shifted, yielding a broader frequency range of operation. This also allows a variable phase response, which can be programmed across the surface to realize real-time beamforming. As is evident from the physical x - y symmetry of the structure, this unit cell demonstrates an identical response for x - and y -polarized incident waves (i.e., a dual linearly polarized (LP) behavior). Important design parameters are labeled in Fig. 1 and listed in Table I. Resistors (R) are 25 k Ω bias resistors operating as chokes for the RF signals, and the substrate is Rogers RO4003 with a thickness of 0.8128 mm, permittivity of $\epsilon_r = 3.55$ and a loss tangent of $\tan \delta = 0.0027$. The geometric parameters in Table I have been obtained by an initial calculation of the radii of the two rings such that they are resonant at the upper frequency limit of each operating band, and as such, the addition of the capacitive loading would reduce the resonance frequency for obtaining S-curves at lower frequencies within each band. Thereafter, the design parameters are fine-tuned using parametric studies in Ansys HFSS.

The unit cell period is chosen such that grating lobes are prevented for maximum beam scan angles of $\pm 50^\circ$ at the operating frequency of 14.5 GHz. As such, the maximum spacing for a rectangular grid may be calculated as

$$d = \frac{\lambda}{1 + \sin(\theta_{max})}, \quad (1)$$

while for a triangular grid the maximum spacing is obtained as [33]

$$d = 1.15 \frac{\lambda}{1 + \sin(\theta_{max})}. \quad (2)$$

Therefore, a triangular grid allows 15% larger spacing between the unit cells compared to a rectangular grid for achieving the same maximum scan angle without grating lobes. This enables reducing the number of elements in the array (and therefore the cost) for a fixed overall size, which is an important consideration when using active devices such as varactor diodes.

Fig. 2(a) represents the elements of the lower band placed in an interleaved manner in a triangular grid; the elements of the upper band are then inserted at the corners, as demonstrated in Fig. 2(b). This results in the trapezoidal unit cell geometry

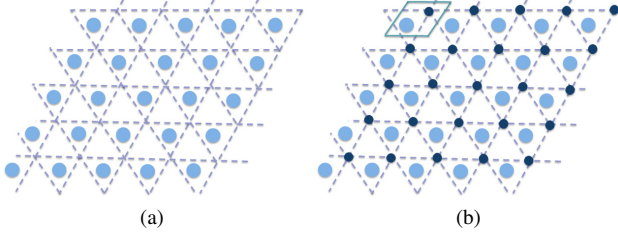


Fig. 2. The proposed triangular grid with (a) interleaved elements of the lower frequency band and (b) the elements of the upper frequency band inserted at the corners.

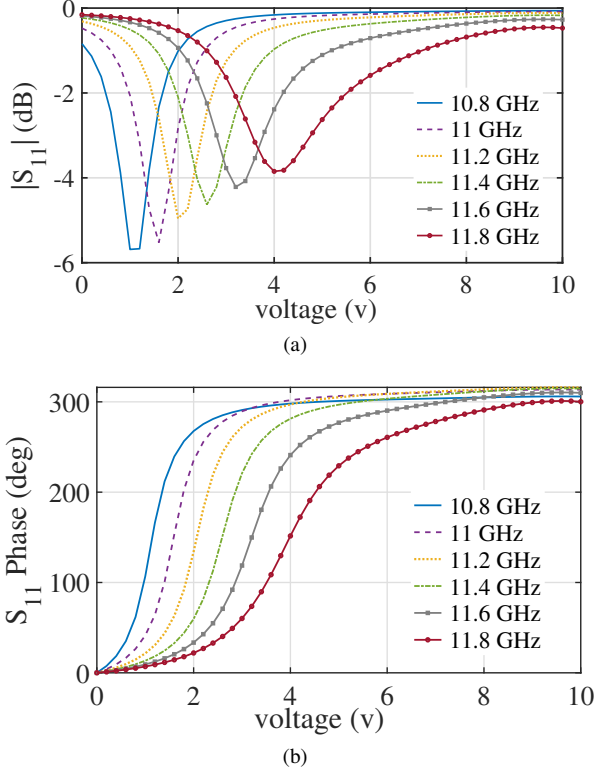


Fig. 3. Simulated (a) magnitude and (b) phase of the reflection parameter at different frequencies within the lower band plotted as a function of bias voltage.

that was shown in Fig. 1, which may be modeled and studied through periodic boundary conditions.

III. UNIT CELL SIMULATIONS

A. Lower Band

Full-wave simulations of the proposed unit cell are carried out in Ansys HFSS using periodic boundary conditions. The circuit model for the lumped-component varactor diodes as well as details on the voltage-capacitance relationship can be found in the datasheet of the components [32], which has been applied via a post processing step to compute the scattering parameters as the loading capacitance is varied. This post-processing step is carried out by constructing a 10 by 10 scattering matrix, wherein two of the ports refer to the two orthogonal propagating Floquet harmonics, and the other 8 ports represent the 8 varactor diodes in one unit cell. The multi-Floquet-port simulation is carried out once

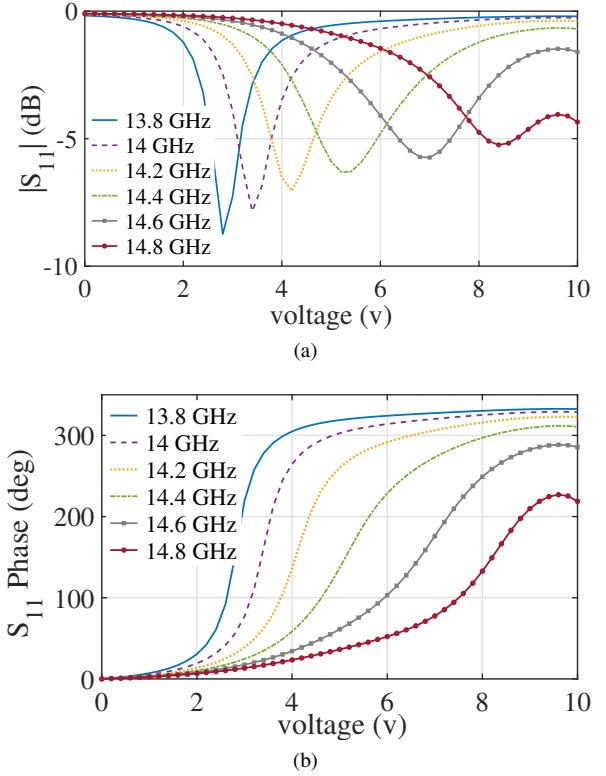


Fig. 4. Simulated (a) magnitude and (b) phase of the reflection parameter at different frequencies within the upper frequency band plotted versus the bias voltage.

with the power fed to port 1, and the scattering data are extracted. Thereafter, the ports representing the varactors are loaded using the aforementioned circuit model in the post-processing of the obtained multi-port matrix [34]. Modeling the discrete variable elements by such internal ports and post-processing allows drastic reduction of the computation time. The magnitude and phase of the reflection coefficient are accordingly derived from unit cell simulations excited at normal incidence with two linearly polarized waves at different frequencies within the lower band as the voltage applied to the varactor diodes is varied. Series varactor parasitics, including an inductance $L = 0.2$ nH and resistance $R = 1.6$ Ω are also accounted for when obtaining the magnitude and phase of the reflection parameter. The corresponding data are shown in Fig. 3. The data demonstrated in Fig. 3(a) indicate an average loss of about 2 dB in the magnitude of the reflection parameter at different design frequencies. A phase range of about 300° is shown to be obtained at different frequencies in the lower band as the bias voltage and therefore the capacitance of the varactor diodes is varied in Fig. 3(b).

B. Upper Band

The magnitude and phase of the reflection parameter are obtained through full-wave HFSS simulations at different frequencies within the upper band in a similar manner, and plotted in Fig. 4 as a function of the bias voltage. The magnitude curves of the reflection parameter shown in Fig. 4(a) imply an average loss of 3 dB at different design frequencies within the upper band, while the phase data in Fig. 4(b)

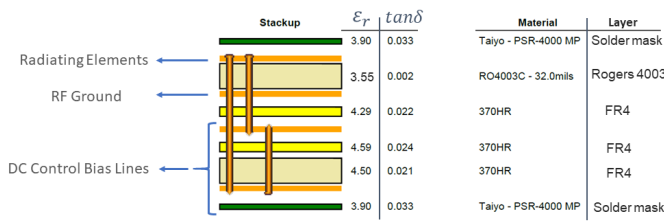


Fig. 5. Layers of the fabricated prototype.

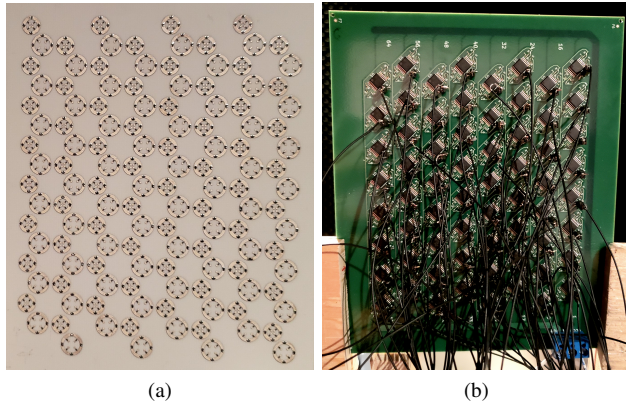


Fig. 6. (a) Front and (b) back views of the fabricated 8 by 8 RA.

demonstrate more than 300° of phase range as the bias voltage is varied.

IV. FABRICATION

To verify the beam scanning response, a small 8 by 8 array was fabricated for proof-of-concept measurements. The printed circuit board was designed to include four layers as pictured in the diagram shown in Fig. 5. The top-most layer contains the radiating elements. RF ground resides on the second layer, while the DC control bias lines are placed on the third and fourth layers.

The front and back views of the fabricated prototype are shown in Fig. 6(a) and 6(b) picturing the radiating elements and the bias network, respectively. The control system consists of USB data-acquisition (DAQ) devices from Measurement Computing (USB-3114) wherein the analog output-voltage terminals are capable of providing analog output voltage values in the range of [0-10] V. To expand the range of voltage values, operational amplifiers (op-amps) with a gain of 4 are used in the bias network. The analog output-voltage terminals from the USB-3114 DAQ devices are connected to the input of the op-amps, which amplify the applied voltage and apply it to the varactor diodes.

There are 64 op-amp ICs in the bias network [35], wherein each IC controls the voltage applied to one unit cell. There are four op-amps within each IC, two of which are connected to each ring inside one unit cell, where one is used in an inverting configuration and another in a non-inverting configuration. This produces the voltage outputs of $+V_b$ and $-V_b$, which are applied to one ring along with two RF ground voltages

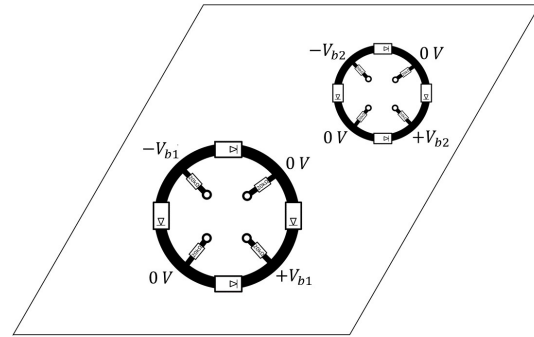


Fig. 7. The biasing scheme for one unit cell.

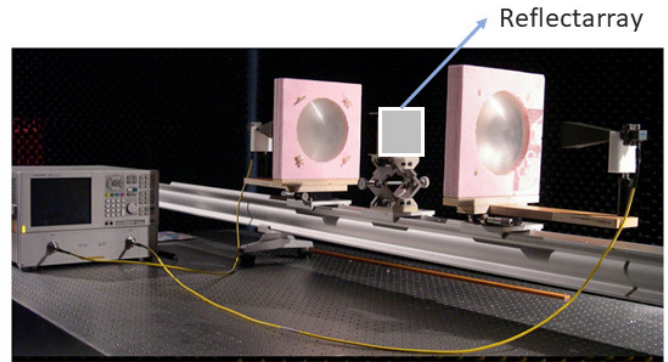


Fig. 8. A quasi-optical measurement system [36].

such that the four varactor diodes share the identical bias voltage of V_b . The biasing scheme for one unit cell is shown in Fig. 7, with V_{b1} and V_{b2} referring to the bias voltage in the lower and upper bands, respectively. The DAQ devices are programmed using the corresponding toolbox in MATLAB, providing identical voltage values to varactors inside each ring in one unit cell, while the applied voltages can vary from one unit cell to another so as to apply the desired phasing scheme.

V. EXPERIMENTAL VALIDATION

A. Quasi-Optical Measurements

To characterize the unit cell characteristics of the fabricated RA, the array is biased uniformly at first to obtain the magnitude and phase of the reflection parameter versus the bias voltage through measurements in a quasi-optical system. This measurement system is shown in Fig. 8 and is composed of two conical horn antennas connected to the ports of a vector network analyzer as well as two collimating lenses that focus the beam radiated from the horns onto a desired beam waist. The lens radii and spacings are designed here such that they focus the beam radiated from the horns into a desired beam waist (~ 7 cm) on the RA, over which the fields resemble those of a plane wave. Since S_{11} is measured here, only half of this measurement system is used. Furthermore, a TRL calibration is required prior to the measurements [36]. The setup is vectorial, and the LP components of the reflection parameter are measured to construct the CP response.

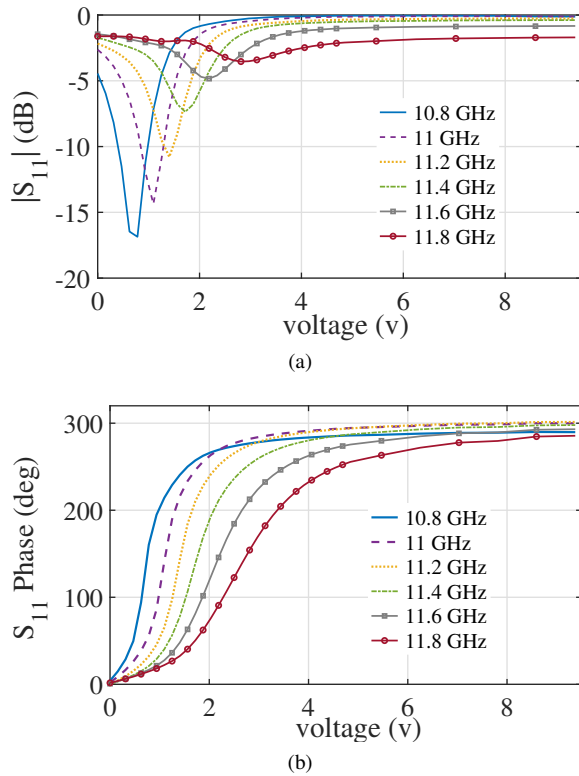


Fig. 9. Measured (a) magnitude and (b) phase of the reflection parameter at different frequencies within the lower band.

1) *Lower Band*: The amplitude and phase responses for the frequencies within the lower band are measured using this quasi-optical setup and depicted in Fig. 9. Small deviations are observed in the trend between the simulated data previously shown in Fig. 3 and the measured data, which could be caused by inaccuracies of the capacitance versus voltage function used to model the varactor diodes in simulations. In addition, more loss effects are observed in the quasi-optical measurements compared to the simulations; nonetheless, our near-field measurement scans (discussed next) yield gain values that are consistent with the simulated loss of the RA unit cell. As such, the increased loss levels observed in the quasi-optical measurements are likely to be caused by the small size of the fabricated RA as well as potential misalignment of the quasi-optical measurement system. Fabrication errors may also be responsible for slight shifts in the resonance frequency, which can shift the S_{11} response and induce more losses.

2) *Upper Band*: The measured magnitude and phase responses in the upper band are shown in Fig. 10, which present similar trends and phase ranges to the corresponding simulated data (Fig. 4), except for a general frequency upshift. Both higher than expected parasitic capacitance and inductance can contribute to this frequency shift, whose effects are expectedly more pronounced at higher frequencies. The measured amplitude data also show higher-than-expected losses similar to the data obtained in the lower-band; nonetheless, and as was argued before, the data from quasi-optical tests seem to be overestimating the amount of loss, and the near-field measurement gain calculations discussed later in Sec. V.B consistently imply a degree of unit-cell loss that aligns with

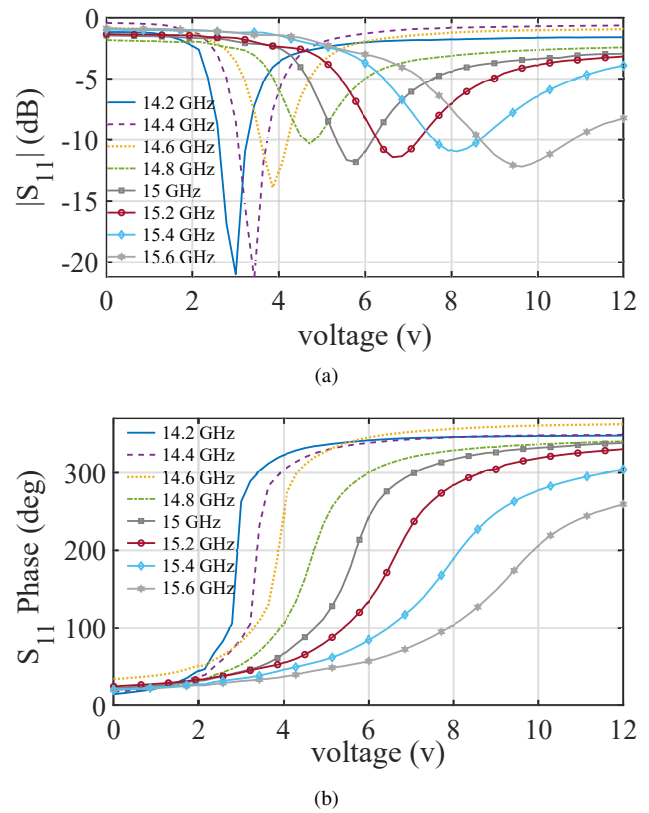


Fig. 10. Measured (a) magnitude and (b) phase of the reflection parameter at different frequencies within the upper frequency band, obtained through quasi-optical measurements.

those suggested by the simulations.

Although this design is not wideband enough to cover the entire intended bands, the unit cell can be further optimized in future work to address this issue. In fact, the uplink satellite communication in the Ku band traditionally takes place in the frequency range of [13.75 – 14.5] GHz, and in practice, sometimes a smaller frequency range of [14 – 14.5] GHz is used, where a 500 MHz bandwidth would suffice. As such, the proposed unit cell is wideband enough in the upper band, except for a frequency shift that can be compensated for upon a more accurate model for varactor diodes to better account for parasitic effects during the design step. However, the total required bandwidth in the downlink band is about 2 GHz ([10.7 – 12.75] GHz), and it has proven difficult to cover the entire band. Therefore, further optimization of the unit cell is necessary before a prototype with improved downlink bandwidth can be designed.

B. Far-Field Response

Figure 11 depicts the planar near-field scan setup in an anechoic chamber, picturing the X-band pyramidal horn antenna (feed) from A-INFO Inc. with a gain of 20 dB and the WR-90 waveguide probe (receiving antenna) on the right-hand side, and the RA accompanied by its control network on the left-hand side of the picture. A focal distance of 45 cm is used, indicating an f/D ratio of 4. This f/D ratio, however, is not indicative of the final value due to the small size of the

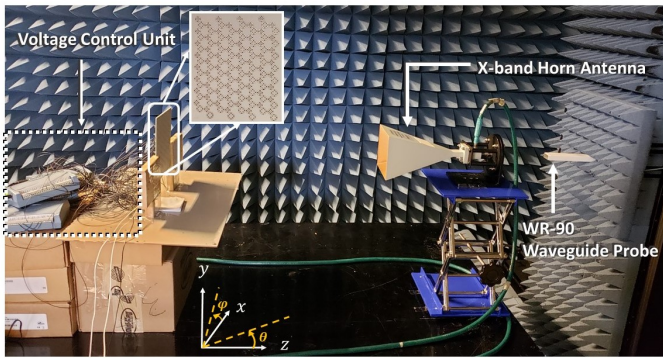


Fig. 11. The experiment setup inside a near-field anechoic chamber picturing the feed (X-band horn), RA under test, as well as the receiving antenna (WR-90 waveguide probe).

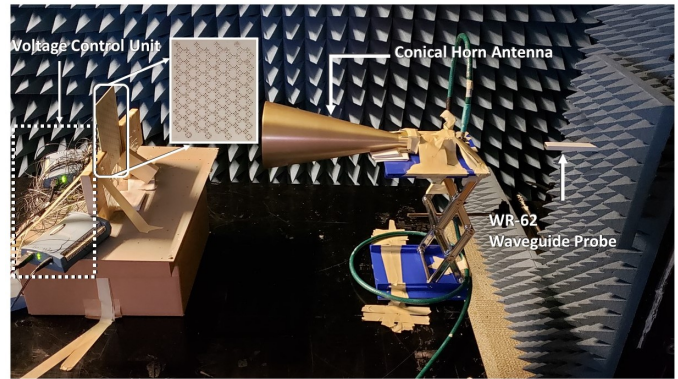


Fig. 13. The experiment setup inside a near-field anechoic chamber picturing the feed (conical horn antenna), RA, and the receiving antenna (WR-62 waveguide probe).

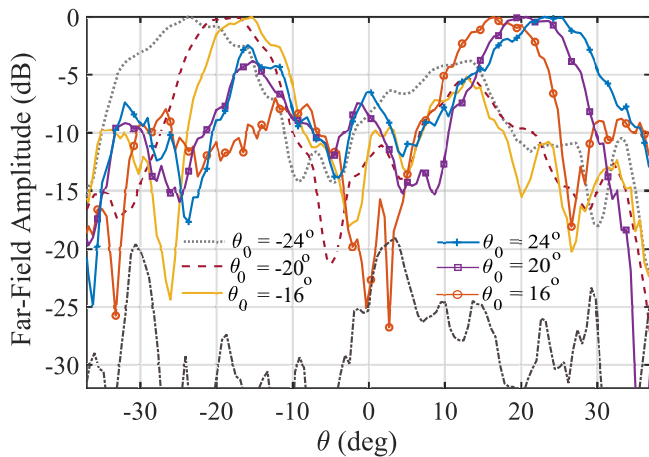


Fig. 12. Response of the proposed RA for various scan angles at the design frequency of 11.2 GHz located in the lower frequency band. Cross-polarized pattern for the representative case of $\theta = -16^\circ$ has been added for comparison in the dash-dotted black curve.

fabricated prototype. The X-band horn covers the lower end of the Ku band and was characterized at frequencies located within the lower operating band of the RA.

Multiple measurements were carried out for different scan angles at the representative design frequency of 11.2 GHz within the lower band to show the beam-steering capability of the fabricated prototype. The measurements were conducted for two linearly polarized incident waves and post-processed to represent the CP response. To do so, the RA is first excited with an x -directed electric field E_x , and the corresponding far-field data are obtained ($E_{r,x}$). Thereafter, the feed antenna is rotated so as to illuminate the RA with E_y , and the corresponding far-field data are stored again ($E_{r,y}$). The far-field data are then superimposed using an $E_{r,x} \pm jE_{r,y}$ relationship to model illumination from a CP feed. It is important to note that the choice of a $+$ or $-$ sign in the post-processing step is arbitrary, and would depend on the sense of the illuminating CP wave (RHCP or LHCP).

Given the small size of the fabricated panel and the relatively large size of the feed antenna, the focal distance between

the feed and the RA must be chosen such that it is large enough to avoid blockage by the feed for smaller scan angles. A distance of 45 cm was therefore chosen such that beam angles of 15° and higher are not blocked. The large RA-probe separation distance limits the planar measurement setup to a 38° angular range in the azimuthal plane.

Prior to measurements, the X-band conical horn is simulated in order to obtain the incident phase profile; the required phase at each unit cell is then calculated so as to compensate for the nonuniform incident phase and steer the beam to the desired angle according to [1]

$$\psi_{mn} = -\psi_{inc} - k_0 (x'_{mn} \sin(\theta_0) \cos(\phi_0) + y'_{mn} \sin(\theta_0) \sin(\phi_0)), \quad (3)$$

where k_0 is the free-space wave number, x'_{mn} and y'_{mn} refer to the coordinates of each unit cell, and (θ_0, ϕ_0) refer to the scan angles in spherical coordinates. The coordinate system is shown on the bottom-left side of Fig. 11 for reference.

The calculated phases are then mapped onto the design voltages using the phase curves obtained from quasi-optical measurements and previously shown in Fig. 9(b). Here, the RA is phased to produce a beam at different scan angles (θ_0) in the x - z plane (i.e., $\phi = 90^\circ$) at 11.2 GHz. The normalized far-field response of the RA for different scan angles is shown in Fig. 12. The aforementioned angular-span limitation of the planar scanner imposes a constraint on the maximum scan angle that can be accurately verified, determined by the scan angle (θ_0) and half-power beamwidth. Therefore, some widening of the beam is observed for bigger scan angles due to the truncation of the near-field data. Nonetheless, it is shown that the direction of the beam can be precisely controlled through the continuously tunable response of the unit cell. It should be emphasized that these measurements serve as proof-of-concept for verifying the beam-steerable response of the proposed RA, but larger sidelobe levels and high spillover losses are unavoidable due to the small size of the fabricated prototype. The proposed RA should be able to steer the beam anywhere from -50° to 50° in both azimuth and elevation planes.

The experimental setup for the upper band measurements is

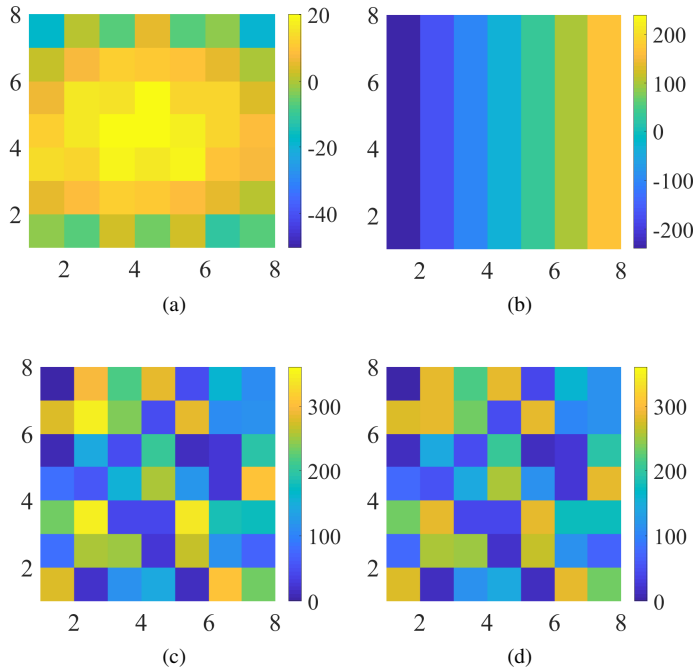


Fig. 14. The profile of (a) incident phases, (b) phases required for steering the beam to $\theta_0 = -18^\circ$ at 15.2 GHz in the x - z plane, (c) total required phases, and (d) achieved design phases on the surface of the RA. All phases are plotted in degrees.

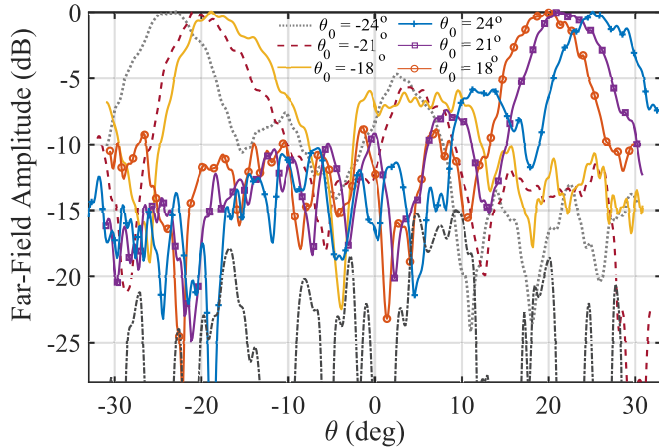


Fig. 15. Response of the proposed RA for various scan angles at the design frequency of 15.2 GHz located in the upper frequency band. Cross-polarized pattern for the representative case of $\theta = -18^\circ$ has been added for comparison in the dash-dotted black curve.

shown in Fig. 13, wherein the feed (conical horn antenna) and the WR-62 waveguide probe (receiving antenna) are located on the right-hand side, while the RA accompanied by its control network is labeled and shown on the left-hand side of the picture. A different feed antenna is used here, which operates at frequencies up to 16 GHz providing a gain of 24 dB. Similar to the measurements carried out in the lower frequency band, multiple measurements are conducted for different scan angles at the representative design frequency of 15.2 GHz within the upper frequency band. A similar focal

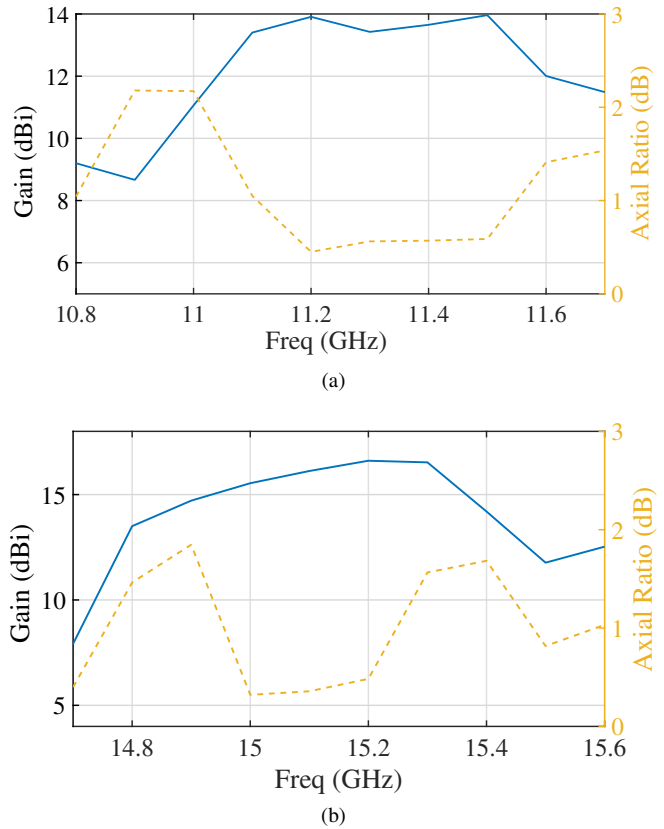


Fig. 16. Gain and AR of the proposed RA versus frequency at (a) $\theta = -16^\circ$ for the design frequency of 11.2 GHz within the lower frequency band and (b) $\theta = -18^\circ$ for the design frequency of 15.2 GHz within the upper frequency band.

length of 45 cm is used, and the response of the conical horn is simulated and measured in order to obtain the incident phase profiles prior to measurements. The calculated phases for beamsteering are mapped onto the design voltages using the phase curves obtained from quasi-optical measurements (shown in Fig. 10(b)). The corresponding profiles of incident phases, phases required for beamsteering for the representative case of $\theta = -18^\circ$, total required phases as well as the final design phases on the surface of the RA are shown in Fig. 14 as an example. The average phase error induced by a 6-bit quantization scheme and a phase range slightly short of 360° is very low (around 6°). This value does not account for any phase errors that are induced by inaccuracies in the measured QO data due to the small size of the prototype or potential misalignment of the setup.

The normalized far-field response of the RA for different scan angles is shown in Fig. 15. The data obtained from these measurements serve as proof-of-concept for verifying the beam-steerable response of the proposed RA at the upper frequency band.

Gain of the RA is calculated for representative measurement cases of $\theta = -16^\circ$ and $\theta = -18^\circ$ in the lower and upper frequency bands, respectively, and the obtained values are plotted in Fig. 16 versus frequency. Smaller scan angles are chosen for gain calculations wherein the measured data are expected to be more accurate due to the sufficient distance between the center of the beam and edge of the scan window,

which allows for proper taper in the near-field measurement data.

Fig. 16(a) demonstrates a maximum gain of 13.98 dBi at the design frequency of 11.2 GHz. The gain drops away from the design frequency due to introduction of phase errors; nonetheless, a 1-dB instantaneous gain-bandwidth of 500 MHz is obtained. The gain data in Fig. 16(b) demonstrate a maximum gain of 16.61 dB at the design frequency of 15.2 GHz, where a 1-dB gain-bandwidth of 350 MHz is obtained. This lower gain-bandwidth is due to the increased phase sensitivity in the upper band caused by frequency shifts, and may be improved by refining the design to compensate for the observed shifts. Figs. 16(a) and 16(b) also show how the axial ratio (AR) varies versus frequency in each operating band (dashed yellow curves). Although AR increases away from the design frequency in each band, it is sufficiently low, and remains below 2.2 dB in Fig. 16(a) and below 2 dB in Fig. 16(b) over the entire corresponding operating bands.

Table II presents the details of the gain budget analysis, including the theoretical maximum gain as well the details on various sources of loss in both frequency bands. The theoretical maximum gain is calculated based on the directivity expected from an aperture antenna of the same overall size as the region occupied by the elements on the RA (96 mm by 112 mm). The average unit cell loss is calculated from simulation data, and the scan loss is calculated as $10 \log(\cos(\theta_0))$ to account for the effective reduction in the aperture size of the antenna as we scan away from the broadside. Taper loss accounts for losses occurred due to the non-uniform excitation amplitudes from the center to the edges of the array. This loss has been calculated by comparing the directivity from an 8 by 8 array under uniform illumination and that obtained under actual illumination amplitudes from the feed (horn) antenna in each band. Spillover losses occur due to the small size of the prototype, causing it not to capture the entire illumination power. This loss is therefore calculated by comparing the total incident power from the feed and comparing it to the portion incident on the surface of the reflectarray. The amplitude profile of incident fields obtained from full-wave simulations of the feed antennas are used for the calculation of taper and spillover losses in each band. As is evident from Table II, the peak measured gains in both bands are very close to the expected maximum value from theoretical calculations. It also is evident from Table II that spillover is a major source of loss; nonetheless, these losses could be mitigated to some extent by using a different, smaller feed antenna that would allow smaller spacing between the feed and the RA without causing blockage concerns, or by fabricating a larger RA prototype.

Table III lists the measured values for AR at different scan angles within the lower and upper bands that were previously shown in Figs. 12 and 15. The value of AR is sufficiently low in all the measurements, indicating a very low level of cross polarization.

Table IV shows a comparison between different properties of the proposed structure and other recent reconfigurable RA antennas proposed in the literature. A comparison has been carried out in terms of the number of operating bands (single or dual), polarization (linear, circular), axial ratio (for CP

TABLE II
GAIN BUDGET ANALYSIS AT 11.2 GHz AND 15.2 GHz.

Source of Loss	$f = 11.2$ GHz	$f = 15.2$ GHz
Average unit cell loss	2 dB	3 dB
Scan loss	0.17 dB	0.22 dB
Taper loss	1.35 dB	0.1 dB
Spillover loss	4.95 dB	5.655 dB
Total loss	8.46 dB	8.9 dB
Maximum aperture directivity	22.7 dBi	25.4 dBi
Theoretical peak gain	14.28 dBi	16.49 dBi
Measured peak gain	13.98 dBi	16.61 dBi

TABLE III
AXIAL RATIO (AR) FOR DIFFERENT SCAN ANGLES AT 11.2 GHz AND 15.2 GHz.

θ_0 at 11.2 GHz	AR (dB)	θ_0 at 15.2 GHz	AR (dB)
$\theta_0 = -24^\circ$	1.08 dB	$\theta_0 = -24^\circ$	1.06 dB
$\theta_0 = -20^\circ$	0.97 dB	$\theta_0 = -21^\circ$	0.65 dB
$\theta_0 = -16^\circ$	0.45 dB	$\theta_0 = -18^\circ$	0.48 dB
$\theta_0 = 16^\circ$	0.75 dB	$\theta_0 = 18^\circ$	0.74 dB
$\theta_0 = 20^\circ$	1.03 dB	$\theta_0 = 21^\circ$	0.71 dB
$\theta_0 = 24^\circ$	1.38 dB	$\theta_0 = 24^\circ$	1.31 dB

antennas), percentage gain-bandwidth, average unit-cell loss, as well as the ability to steer the beam in a continuous manner. As the information in the table implies, this work is the first demonstration of a dual-band, CP, *continuously* tunable RA antenna in the literature. Average unit-cell loss is comparable to other RA antennas relying on varactor diodes to achieve continuous tunability, and a decent axial ratio is obtained owing to the symmetric profile of the unit cell. The 1- or 3-dB gain-bandwidths are also reported for some of the references in the table that had provided the data, which are accompanied by the electrical size of the array. The gain-bandwidth in this work is comparable to the other works in the literature that can continuously steer the beam. For dual-band designs, the electrical size is reported at the design frequency in the upper frequency band. The 3-dB gain bandwidth in this work measures the values of 7.6% and 4.3% in the lower and upper bands, respectively.

VI. CONCLUSIONS

In this work, a dual-band dual-CP fully reconfigurable RA antenna is introduced for use in ground base-stations of satellite communication systems. It was shown through full-wave simulations and proof-of-concept measurements of a fabricated prototype that the proposed RA can provide independent and continuous beam-steering in both downlink and uplink frequency bands. The gain of the RA was measured versus frequency for representative design frequencies and beam scan angles within both bands, which were shown to be consistent with the expected peak gain after taking unit cell/spillover/taper and scan losses into account. A 1-dB gain-bandwidth of about 500 MHz and 350 MHz were obtained in the lower and upper bands, respectively. In addition, axial ratio values smaller than 1.38 dB are obtained at all scan angles and test frequencies, indicating an isotropic response and low levels of cross polarization. Some frequency shifts are observed especially in the upper frequency band (up to

TABLE IV
PROPERTIES OF THE PROPOSED RA VERSUS OTHER RECENT RAS

Ref.	Dual Band	Polarization	AR (dB)	G-BW (1 or 3dB) (Size)	Loss (dB)	Cont. Beam-steering
[15]	No	Linear	N/A	Not provided	1.5	No
[16]	No	Circular	2	Not provided	1.8	No
[17]	No	Circular	Not provided	Not provided	0.6	No
[18]	No	Circular	Not provided	Not provided	0.5	No
[19]	No	Linear	N/A	2.4% (1-dB) (80λ by 32λ)	1.15	No
[20]	No	Linear	N/A	10% (1-dB) (11λ by 11λ)	0.5	No
[22]	No	Linear	N/A	4.4% (1-dB) (3.1λ by 3.1λ)	2.41	Yes
[23]	No	Linear	N/A	3.6% (3-dB) (3.3λ by 4λ)	2.1	Yes
[24]	Yes	Circular	Not provided	Not provided	Very low	No
[25]	Yes	Circular	Not provided	Not provided	3	No
[26]	Yes	Linear	N/A	11.6, 11.9% (3-dB) (8λ by 8λ)	0.5-1	No
This work	Yes	Circular	0.48	4.5, 2.3% (1-dB) (4.9λ by 5.7λ)	3	Yes

4%), which can be mitigated through a more accurate model for parasitics introduced by the varactor diodes. Other factors such as fabrication errors and material tolerances may also have contributed to the observed frequency shifts.

This antenna is a suitable candidate for use in ground base stations of satellite communications systems for communication with low-earth-orbit satellites in the Ku band due to its capability for simultaneous transmit/receive operation, fast and versatile beam-steering in a fully continuous angular range, as well as its lightweight profile and dual-CP response. The continuous voltage-control scheme used here allows for any tuning resolution of interest without additional hardware complexity as well as precise control over the scan angle. The varactor diodes do not consume bias current, allowing for low-power control of the beam.

REFERENCES

[1] S. V. Hum and J. Perruisseau-Carrier, "Reconfigurable reflectarrays and array lenses for dynamic antenna beam control: A review," *IEEE Trans. Antennas Propag.*, vol. 62, no. 1, pp. 183–198, 2013.

[2] E. Carrasco, J. A. Encinar, and Y. Rahmat-Samii, "Reflectarray antennas: A review," in *Forum for Electromagnetic Research Methods and Application Technologies (FERMAT)*, vol. 16, 2016.

[3] A. E. Martynyuk, J. M. Lopez, and N. A. Martynyuk, "Spiraphase-type reflectarrays based on loaded ring slot resonators," *IEEE Trans. Antennas Propag.*, vol. 52, no. 1, pp. 142–153, 2004.

[4] S. Mener, R. Gillard, R. Sauleau, A. Bellion, and P. Potier, "Dual circularly polarized reflectarray with independent control of polarizations," *IEEE Trans. Antennas Propag.*, vol. 63, no. 4, pp. 1877–1881, 2015.

[5] R. Deng, Y. Mao, S. Xu, and F. Yang, "A single-layer dual-band circularly polarized reflectarray with high aperture efficiency," *IEEE Trans. Antennas Propag.*, vol. 63, no. 7, pp. 3317–3320, 2015.

[6] T. Smith, U. Gothelf, O. S. Kim, and O. Breinbjerg, "Design, manufacturing, and testing of a 20/30-GHz dual-band circularly polarized reflectarray antenna," *IEEE Antennas Wireless Propag. Lett.*, vol. 12, pp. 1480–1483, 2013.

[7] R. Deng, F. Yang, S. Xu, and M. Li, "An fss-backed 20/30-GHz dual-band circularly polarized reflectarray with suppressed mutual coupling and enhanced performance," *IEEE Trans. Antennas Propag.*, vol. 65, no. 2, pp. 926–931, 2016.

[8] X.-J. Zhong, L. Chen, Y. Shi, and X.-W. Shi, "A novel design of dual broadband, single-layer circularly polarized reflectarray," *International Journal of RF and Microwave Computer-Aided Engineering*, vol. 25, no. 4, pp. 364–369, 2015.

[9] C. Han, C. Rodenbeck, J. Huang, and K. Chang, "AC/Ka dual frequency dual layer circularly polarized reflectarray antenna with microstrip ring elements," *IEEE Trans. Antennas Propag.*, vol. 52, no. 11, pp. 2871–2876, 2004.

[10] Z. H. Jiang, T. Yue, and W. Hong, "Low-profile and wideband dual-circularly polarized reflect-arrays based on rotated metal-backed dual-polarized aperture-coupled patch elements," *IEEE Trans. Antennas Propag.*, vol. 68, no. 3, pp. 2108–2117, 2019.

[11] R. E. Munson, H. A. Haddad, and J. W. Hanlen, "Microstrip reflectarray for satellite communication and radar cross-section enhancement or reduction," Aug. 4 1987, uS Patent 4,684,952.

[12] Q. Luo, S. Gao, W. Li, M. Sobhy, I. Bakaimi, C. K. de Groot, B. Hayden, I. Reaney, and X. Yang, "Multibeam dual-circularly polarized reflectarray for connected and autonomous vehicles," *IEEE Trans. Veh. Technol.*, vol. 68, no. 4, pp. 3574–3585, 2019.

[13] S. Mener, R. Gillard, R. Sauleau, C. Cheymol, and P. Potier, "Unit cell for reflectarrays operating with independent dual circular polarizations," *IEEE Antennas Wireless Propag. Lett.*, vol. 13, pp. 1176–1179, 2014.

[14] C. Zhang, Y. Wang, F. Zhu, G. Wei, J. Li, C. Wu, S. Gao, and H. Liu, "A planar integrated folded reflectarray antenna with circular polarization," *IEEE Trans. Antennas Propag.*, vol. 65, no. 1, pp. 385–390, 2016.

[15] H. Rajagopalan, Y. Rahmat-Samii, and W. A. Imbriale, "RF MEMS actuated reconfigurable reflectarray patch-slot element," *IEEE Trans. Antennas Propag.*, vol. 56, no. 12, pp. 3689–3699, 2008.

[16] L. Martinez-Lopez, J. Rodriguez-Cuevas, A. E. Martynyuk, and J. I. Martinez-Lopez, "Wideband-reconfigurable reflectarrays based on rotating loaded split rings," *J. Electromagn. Waves Appl.*, vol. 29, no. 2, pp. 218–232, 2015.

[17] T. Debogovic and J. Perruisseau-Carrier, "Low loss MEMS-reconfigurable 1-bit reflectarray cell with dual-linear polarization," *IEEE Trans. Antennas Propag.*, vol. 62, no. 10, pp. 5055–5060, 2014.

[18] S. Mener, R. Gillard, R. Sauleau, C. Cheymol, and P. Potier, "Design and characterization of a CPSS-based unit-cell for circularly polarized reflectarray applications," *IEEE Trans. Antennas Propag.*, vol. 61, no. 4, pp. 2313–2318, 2012.

[19] X. Pan, F. Yang, S. Xu, and M. Li, "A 10240-element reconfigurable reflectarray with fast steerable monopulse patterns," *IEEE Trans. Antennas Propag.*, 2020.

[20] E. Carrasco, M. Barba, and J. A. Encinar, "X-band reflectarray antenna with switching-beam using PIN diodes and gathered elements," *IEEE Trans. Antennas Propag.*, vol. 60, no. 12, pp. 5700–5708, 2012.

[21] S. V. Hum, M. Okoniewski, and R. J. Davies, "Modeling and design of electronically tunable reflectarrays," *IEEE Trans. Antennas Propag.*, vol. 55, no. 8, pp. 2200–2210, 2007.

[22] M. E. Trampler, R. Lovato, and X. Gong, "Dual-resonance continuously beam-scanning X-band reflectarray antenna," *IEEE Trans. Antennas Propag.*, 2020.

[23] M. Riel and J.-J. Laurin, "Design of an electronically beam scanning reflectarray using aperture-coupled elements," *IEEE Trans. Antennas Propag.*, vol. 55, no. 5, pp. 1260–1266, 2007.

[24] C. Guclu, J. Perruisseau-Carrier, and O. Civi, "Proof of concept of a dual-band circularly-polarized RF MEMS beam-switching reflectarray," *IEEE Trans. Antennas Propag.*, vol. 60, no. 11, pp. 5451–5455, 2012.

[25] Q. Luo, S. Gao, Y. Wang, I. Bakaimi, A. Mostaed, C. K. de Groot, B. Hayden, and I. Reaney, "Electronically beam-steerable dual-band reflectarray for satellite communications," in *2019 IEEE-APS Topical Conference on Antennas and Propagation in Wireless Communications (APWC)*. IEEE, 2019, pp. 050–055.

[26] H. Xu, S. Xu, F. Yang, and M. Li, "Design and experiment of a dual-band 1-bit reconfigurable reflectarray antenna with independent large-angle beam scanning capability," *IEEE Antennas Wireless Propag. Lett.*, 2020.

[27] A. Clemente, F. Diaby, L. Di Palma, L. Dussopt, and R. Sauleau, "Experimental validation of a 2-bit reconfigurable unit-cell for transmitarrays at Ka-band," *IEEE Access*, vol. 8, pp. 114991–114997, 2020.

[28] F. Diaby, A. Clemente, L. Di Palma, L. Dussopt, K. Pham, E. Fourn, and R. Sauleau, "Linearly-polarized electronically reconfigurable transmitarray antenna with 2-bit phase resolution in Ka-band," in *2017*

International Conference on Electromagnetics in Advanced Applications (ICEAA). IEEE, 2017, pp. 1295–1298.

- [29] Z. Wang, Y. Ge, J. Pu, X. Chen, G. Li, Y. Wang, K. Liu, H. Zhang, and Z. Chen, “1-bit electronically reconfigurable folded reflectarray antenna based on PIN diodes for wide-angle beam-scanning applications,” *IEEE Trans. Antennas Propag.*, 2020.
- [30] A. R. Vilenkiy, M. N. Makurin, C. Lee, and M. V. Ivashina, “Reconfigurable transmitarray with near-field coupling to gap waveguide array antenna for efficient 2D beam steering,” *IEEE Trans. Antennas Propag.*, 2020.
- [31] E. Baladi, M. Y. Xu, N. Faria, J. Nicholls, and S. V. Hum, “Dual-band circularly-polarized beam-steerable reflectarray for satellite applications in the Ku band,” in *press for publication in the 2020 IEEE International Symposium on Antennas and Propagation (APS/URSI)*. IEEE, 2020.
- [32] “Datasheet for MAVR-011020-1141 varactor diodes, <https://cdn.macom.com/datasheets/mavr-011020-1141.pdf>.”
- [33] A. K. Bhattacharyya, *Phased array antennas: Floquet analysis, synthesis, BFNs and active array systems*. John Wiley & Sons, 2006, vol. 179.
- [34] J. Perruisseau-Carrier, F. Bongard, R. Golubovic-Niciforovic, R. Torres-Sánchez, and J. R. Mosig, “Contributions to the modeling and design of reconfigurable reflecting cells embedding discrete control elements,” *IEEE Trans. Microw. Theory Techn.*, vol. 58, no. 6, pp. 1621–1628, 2010.
- [35] “Datasheet for the op-amp ICs, <https://www.onsemi.com/pub/collateral/mc33178-d.pdf>.”
- [36] A. K. Iyer, “Free-space metamaterial superlenses using transmission-line techniques,” Ph.D. dissertation, 2009.



Elham Baladi (S’15–M’19) received the B.Sc. degree in electrical engineering - communications from the Iran University of Science and Technology, Tehran, Iran, in 2013, and the Ph.D. degree in electromagnetics and microwaves from the University of Alberta, Edmonton, AB, Canada, in January 2019. She investigated antenna miniaturization techniques based on the application of metamaterials and novel metamaterial-loaded resonant metasurfaces during her Ph.D. degree.

Dr. Baladi was a postdoctoral fellow with the University of Toronto, Toronto, ON, Canada, from February 2019 to February 2021, where she conducted research on the modeling and development of reconfigurable metasurfaces and antenna arrays for space applications. She is currently an Antenna and Filter Design Engineer with Syntronic Research and Development Canada. Her research interests include theoretical modeling, design and characterization of multi-band beam-steerable antennas, metasurfaces, reflectarrays, and leaky-wave antennas.

Dr. Baladi was the recipient of the University of Alberta Doctoral Recruitment scholarship, the Alberta Innovates Technology Futures scholarship, the IEEE AP-S Doctoral Research Award, and two honorable mention awards in the student-paper competitions of the 2016 and 2017 IEEE AP-S Symposia. She has been a Member of the IEEE Northern Canada Section since 2013 and the IEEE Antennas and Propagation Society since 2015. She currently serves as a reviewer for IEEE Transactions on Antennas and Propagation, IEEE Transactions on Microwave Theory and Techniques, IEEE Access, and IEEE Antennas and Wireless Propagation Letters.



Nicolas Faria received the B.Sc. degree in electrical engineering from the University of Alberta, Edmonton, AB, Canada, in 2018. He is currently pursuing a M.A.Sc. degree at the University of Toronto, Toronto, ON, Canada. His current research interests include design and characterization of reconfigurable metasurfaces, antennas and frequency-selective surfaces.



Jeff Nicholls (Member, IEEE) received the B.A.Sc. degree in engineering physics and M.A.Sc. degree in electrical engineering from the University of Toronto, Toronto, ON, Canada in 2013 and 2016 respectively. Following his degrees he joined SpaceX in Redmond, Washington, USA as an Antenna Engineer for almost two years. There he contributed to the development of the phased arrays and other antennas for the two pathfinder Starlink satellites Tintin-1a/1b. In 2018 he then joined the small satellite startup Kepler Communications in Toronto, ON, Canada where he started as Lead Antenna Engineer and is now Manager, RF and Antenna Design. His work specializes in communications payload development for small satellites as part of the recent trend in development of low-earth orbit, non-geostationary communication constellations. Jeff’s interests lie predominantly in novel satellite-based communications systems and micro-/mm-wave phased arrays and beamforming.



Sean Victor Hum (S’95–M’03–SM’11) received the B.Sc., M.Sc., and Ph.D. degrees in electrical and computer engineering from the University of Calgary, Calgary, AB, Canada, in 1999, 2001, and 2006, respectively.

In 2006, he joined The Edward S. Rogers Senior Department of Electrical and Computer Engineering, University of Toronto (UofT), Toronto, ON, Canada, where he is currently a Professor and the Eugene V. Polistuk Chair in Electromagnetic Design. He is also the Associate Chair, Graduate Studies in the same department. He leads the Reconfigurable Antenna Laboratory, UofT, and along with his students, conducts research in the areas of reconfigurable/multifunction antennas, space-fed arrays, electromagnetic surfaces, and antennas for space applications.

Dr. Hum was a recipient of the Governor General’s Gold Medal for his work on radio-on-fiber systems in 2001, the IEEE Antennas and Propagation Society Student Paper Award for his work on electronically tunable reflectarrays in 2004, the ASTech Leaders of Tomorrow Award for his work in this area in 2006, the Early Researcher Award by the Government of Ontario in 2012, and the six UofT Departmental Teaching Awards since 2007 and a Faculty Early Career Teaching Award in 2011 for his teaching side. He was a co-recipient of the IEEE Antennas and Propagation Society R. W. P. King Award in 2015 and 2017. He served on the Steering Committee and the Technical Program Committee of the 2010 and 2020 IEEE AP-S International Symposium on Antennas and Propagation. He was the TPC Co-Chair of the 2015 IEEE AP-S International Symposium on Antennas and Propagation. He served as an Associate Editor for the IEEE Transactions on Antennas and Propagation from 2010 to 2017. He is currently co-chair of the IEEE AP-S Education Committee.